

Molecular Origin of Balanced Bipolar Transport in Neat Layers of the Emitter CzDBA

Wenlan Liu, Naresh B. Kotadiya, Paul W. M. Blom, Gert-Jan A. H. Wetzelaer,* and Denis Andrienko*

Recently, an efficient single-layer organic light-emitting diode has been reported, consisting of a neat layer of the diboron-based thermally activated delayed fluorescence emitter 5,10-bis(4-(9H-carbazol-9-yl)-2,6-dimethylphenyl)-5,10-dihydroboranthrene, exhibiting remarkably balanced bipolar electron and hole transport. Here, the donor–acceptor–donor architecture of the molecule is linked to the transport characteristics of its neat amorphous films. It is found that energetic disorder is larger for holes than for electrons, explaining the experimentally observed difference in temperature activation of the mobility. Although a difference in energetic disorder would suggest unbalanced charge transport, it is demonstrated that it is partly counteracted by larger coupling elements for holes.

compound 5,10-bis(4-(9H-carbazol-9-yl)-2,6-dimethylphenyl)-5,10-dihydroboranthrene (CzDBA),^[2] sandwiched between Ohmic electron and hole contacts. The material CzDBA, the chemical structure of which is shown in **Figure 1**, is a donor–acceptor compound, which exhibits thermally activated delayed fluorescence, converting triplet excitons into singlet excitons via reverse intersystem crossing.^[3,4] Part of the success of this single-layer OLED was the near-trap-free and balanced electron and hole transport. As a result, remarkably low operating voltages were obtained, while the external quantum efficiency reached 19%, comparable to multilayer

OLEDs employing triplet-exciton harvesting. Furthermore, the balanced electron and hole transport resulted in a broad recombination zone, leading to greatly enhanced device stability.

With an ionization energy of 5.9 eV and an optical gap of 2.48 eV, the energy levels of CzDBA are located suitably with regard to the recently identified energy window for trap-free charge transport in organic semiconductors.^[5] However, the origin for the *balanced* electron and hole mobility in CzDBA is yet to be explored. In general, charge transport in thermally activated delayed fluorescence (TADF) emitters has been largely ignored, as research has focused more on spectroscopic properties of these materials and their use to create efficient OLEDs. However, understanding of the charge-transport properties is important for developing simplified and more stable TADF-based OLEDs.


In this manuscript, we perform multiscale simulations that yield atomistic morphologies, energy levels, energetic disorder, and charge transport in CzDBA. We additionally perform temperature-dependent charge-transport measurements, to validate the simulations. Interestingly, larger energetic disorder is observed for holes compared to electrons in both simulation and experiment. This difference in energetic disorder is, however, counteracted by an increase in coupling elements for holes, leading to balanced charge transport in CzDBA.

1. Introduction

Design of efficient organic light-emitting diodes (OLEDs) targets several processes simultaneously: balanced electron and hole transport, efficient charge injection, efficient harvesting of both triplet and singlet excitons, and efficient light extraction. A common approach is to dedicate different compounds and layers for each individual process, e.g., dope charge transport layers for Ohmic injection, employ dedicated charge-transport layers to move electrons and holes to the emitting layer, adjust the host for balanced transport inside the emitting layer, and tailor the phosphorescent emitter and host for triplet harvesting. Every new material adds a degree of freedom and hence flexibility to the OLED design, but complicates the final composition of the OLED and may compromise device stability.

Recently, it was demonstrated that such complex multilayer design could be reduced to a simple single-layer architecture.^[1] This was achieved by using a neat layer of the diboron-based

Dr. W. Liu, Dr. N. B. Kotadiya, Prof. P. W. M. Blom, Dr. G.-J. A. H. Wetzelaer, Dr. D. Andrienko
Max Planck Institute for Polymer Research
Ackermannweg 10, Mainz 55128, Germany
E-mail: wetzelaer@mpip-mainz.mpg.de;
denis.andrienko@mpip-mainz.mpg.de

 The ORCID identification number(s) for the author(s) of this article can be found under <https://doi.org/10.1002/admt.202000120>.

© 2020 The Authors. Published by WILEY-VCH Verlag GmbH & Co. KGaA, Weinheim. This is an open access article under the terms of the Creative Commons Attribution License, which permits use, distribution and reproduction in any medium, provided the original work is properly cited.

DOI: 10.1002/admt.202000120

2. Charge Transport Measurements

To explore the charge transport in CzDBA in detail, we have performed temperature-dependent space-charge-limited current measurements on electron- and hole-only devices. Space-charge-limited current measurements give valuable information on the steady-state transport properties, whereas

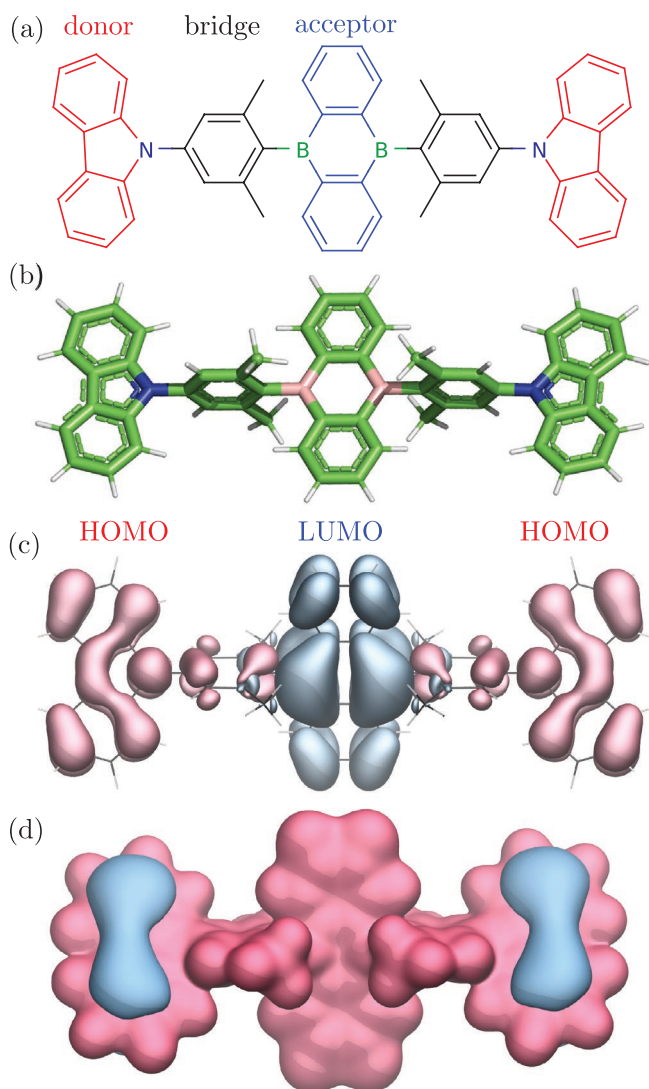


Figure 1. a) Chemical structure, b) optimized geometry (m06-2x/6-311g(d,p)), c) highest occupied molecular orbital (HOMO) and lowest unoccupied molecular orbital (LUMO) orbitals (m06-2x/6-311g(d,p)), d) electrostatic potential (m06-2x/6-311g(d,p) ± 0.03 V) of 5,10-bis(4-(9H-carbazol-9-yl)-2,6-dimethylphenyl)-5,10-dihydroboranthrene, CzDBA.

time-resolved techniques, such as photocurrent time-of-flight measurements can give overestimated mobilities in case of dispersive transport^[6–9] and are insensitive to deep traps.^[10] However, in a space-charge-limited current experiment, it is important to have Ohmic injection from the electrodes, which we have solved here by using a thin interlayer of a material with a large ionization energy.^[11]

Figure 2 displays the temperature-dependent current density–voltage characteristics for electron- and hole-only devices. The experimental data is fitted with drift-diffusion simulations employing the extended Gaussian disorder model (EGDM).^[12] This model describes the mobility in the situation of hopping transport in a system with a Gaussian density-of-states (DOS) distribution and includes the density dependence of the mobility as opposed to original GDM. The EGDM is a mobility function that described the temperature-, density-, and field-dependence of the mobility based on three input parameters, viz. the width of the Gaussian energetic disorder σ , the lattice constant a , and a mobility prefactor μ_0 . By fitting the EGDM to charge-transport measurements at different temperature and layer thicknesses, these three parameters can be reliably determined.^[13–16] Note that due to the small dipole moment (zero in the ground state) of CzDBA, the site energy correlations are small, which justifies the use of the EGDM instead of the correlated Gaussian disorder model.^[17]

As observed in **Figure 2**, the drift-diffusion simulations are in close agreement with the experimental data. Interestingly, even though the electron and hole currents are almost balanced at room temperature, the hole transport exhibits larger temperature dependence. Since the temperature activation of the mobility is controlled by the width of the energetic disorder σ , charge-transport experiments suggest that the energetic disorder for holes is larger than the disorder for electrons. The fit parameters for the EGDM, which are summarized in **Table 1**, indeed confirm this observation. Interestingly, at room temperature the large difference in DOS widths is compensated by the mobility prefactor μ_0 , so that the measured room temperature electron and hole mobilities are well balanced, $\mu_e = 5 \times 10^{-5} \text{ cm}^2 \text{ V}^{-1} \text{ s}^{-1}$, $\mu_h = 3 \times 10^{-5} \text{ cm}^2 \text{ V}^{-1} \text{ s}^{-1}$.

To link energetic disorder and mobility prefactors to the molecular structure, we have simulated atomistic morphologies of CzDBA films, evaluated their solid-state energy levels

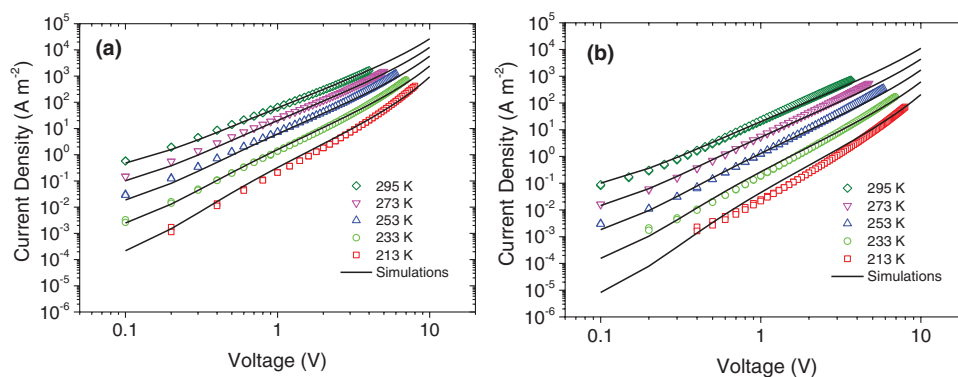


Figure 2. Temperature-dependent current density–voltage characteristics for electrons a) and holes b) in CzDBA single-carrier devices with a CzDBA layer thickness of 130 nm. Symbols represent experimental data, lines are fits with drift-diffusion simulations incorporating the EGDM mobility function.

Table 1. Fit parameters for the EGDM model.

μ_0^e	$5000 \text{ m}^2 \text{ V}^{-1} \text{ s}^{-1}$
μ_0^h	$20\,000 \text{ m}^2 \text{ V}^{-1} \text{ s}^{-1}$
a_e	1.5 nm
a_h	1.3 nm
σ_e	0.115 eV
σ_h	0.135 eV

and the corresponding densities of states, calculated electronic couplings and charge transfer rates, and finally evaluated mobilities of electrons and holes.

3. Charge Transport Simulations

To evaluate the mobilities of amorphous films, we first employed atomistic molecular dynamics simulations to generate the amorphous morphologies. While CzDBA is well aligned in doped host-guest films, with a nematic order parameter of 0.84,^[2] in neat films this alignment is unclear. We therefore study well-defined, orientationally and positionally amorphous morphologies of CzDBA. We then used quantum chemical calculations and polarizable force fields to compute site energies, reorganization energies, and electronic couplings, again as described in the Experimental Section. Using these parameters, we evaluate charge-hopping rates within the high-temperature limit of the Marcus theory. Finally, we employ the kinetic Monte Carlo algorithm to solve the master equation for the drift-diffusion of a hole and electron in the simulated morphologies.

3.1. Morphology

Figure 3 shows the molecular dynamics snapshots of an amorphous morphology, together with the corresponding radial distribution function (RDF). The protocol used to prepare this morphology is described in the Experimental Section. To quantify the structural ordering, we have evaluated the nematic order parameter S , i.e., the largest eigenvalue of the order tensor, $Q_{\alpha\beta} = \left\langle \frac{3}{2} n_\alpha n_\beta - \frac{1}{2} \delta_{\alpha\beta} \right\rangle$, where n is a unit vector along the long molecular axis (we used the normalized vector between the two nitrogen atoms). $S = 1$ corresponds to a morphology of perfectly aligned molecules, $S = 0$ to an isotropic orientational distribution. In our system of density $\rho = 1.074 \text{ g cm}^{-3}$, $S = 0.03$, confirming that we indeed have an amorphous morphology.

The RDF of the simulated amorphous mesophase has two pronounced peaks. Interestingly, the second peak position around 1.5 nm is close to the distance that the EGDM fit predicts for the lattice constant, see Table 1. This clearly indicates that, for anisotropic molecules such as CzDBA, a direct mapping of the atomistically resolved morphology to a cubic lattice model cannot be quantitative.

3.2. Density of States

Solid-state energies of a cation, E_h , anion, E_e , and a neutral state, E_n , where are evaluated as described in the Experimental

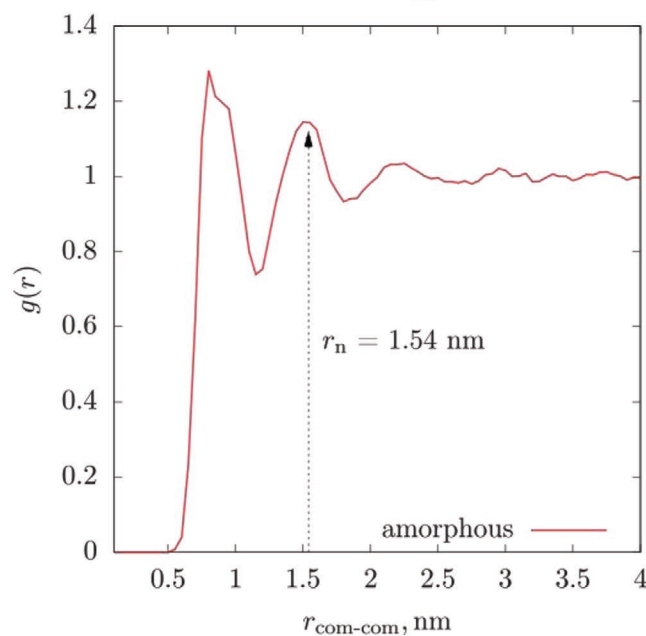
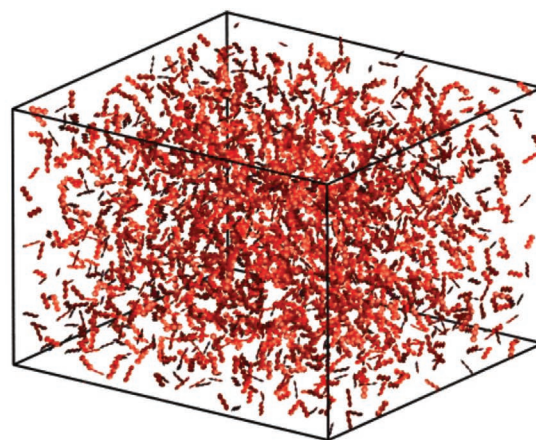


Figure 3. Molecular dynamics snapshot of the amorphous morphology (only DBA cores are shown) and the corresponding radial distribution function based on the molecular centers of masses (com).

Section. From these energies we have calculated the distributions of electron affinities, $EA = E_e - E_n$, and ionization energies, $IE = E_n - E_h$. The onsets of these distributions, $EA_{\text{mean}} - 2\sigma_e$, $IE_{\text{mean}} + 2\sigma_h$, where $\sigma_{e,h}$ are the variances of the Gaussian function fitted to these distributions, can be directly compared to the experimentally measured quantities, in particular the IE measured by the ultraviolet photoelectron spectroscopy (UPS).

Both IE and EA distributions are shown in **Figure 4** together with their onsets, and the gas-phase values. We do observe a good agreement between the simulated (-5.7 eV) and the experimentally measured (-5.9 eV) IEs. Notably, the solid-state stabilization of the cation (1.2 eV) is much larger than the stabilization of the anion (0.8 eV). This asymmetry is the result of a much larger polarizability of the cation as compared to the anion (see the Experimental Section for actual values). It can also be traced back to the molecular architecture: the HOMO is delocalized over the two carbazole donors, while the LUMO is more compact since it is delocalized only over the central DBA unit.

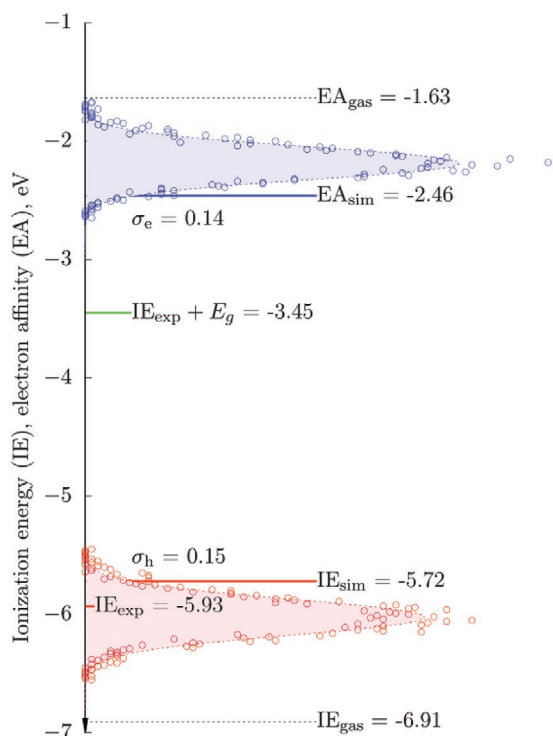


Figure 4. Simulated ionization energy (IE_{sim}) and electron affinity (EA_{sim}) distributions in an amorphous CzDBA film.

In fact, this asymmetry is also important for the balanced *transport* of electrons and holes. Since the donor moieties are free to rotate and therefore are more conformationally disordered than the rigid DBA core, the electrostatic broadening of the IE is much larger than that of the EA (0.18 vs 0.15 eV). However, the larger stabilization of the cation narrows the IE distribution more than the stabilization of the anion narrows the EA distribution. As a result, both distributions have roughly the same width, which is a prerequisite for the balanced bipolar transport.

Another important observation is that the solid-state IE of CzDBA is smaller than 6 eV, which has been reported as the IE above which hole transport becomes trap-limited due to intrinsic impurities, such as water and air.^[5] Similarly, the solid-state IE plus the optical gap, which are often used as an estimate of EA, is around 3.5 eV, which is close to the onset of the trap-limited electron transport.^[18] Hence, both electron and hole transport are not hindered by intrinsic impurities, rendering CzDBA as a bipolar material.

It is also interesting that both calculated and experimentally measured energies of the first excited state are ≈ 1 eV smaller than the transport gap, $EA-IE$. This implies that not only the exchange interaction of the electron and hole but also their direct Coulomb binding is rather small in the first excited state. This is in part due to the spatially separated donor and acceptor and hence electron and hole in the excited state (TADF design). In addition, the dielectric screening of the electron-hole interaction by the polarizable environment is much stronger for excited states with a charge transfer (CT) character.^[19] Indeed, the calculated gas-phase excitation energy of 2.77 eV is ≈ 0.3 eV

off compared to the experimentally measured solid-state optical gap of 2.48 eV, which is a sizable stabilization due to the CT character of the excitation.

3.3. Hole and Electron Mobility

To evaluate the charge transfer rates, we first calculated electron and hole reorganization energies, which amount to $\lambda_e = 0.259$ eV for electrons and $\lambda_h = 0.072$ eV for holes. The much smaller reorganization energy for the hole than for the electron can be explained by analyzing the frontier molecular orbitals, which are shown in Figure 1c. The LUMO is localized on the rigid DBA acceptor where the bond relaxation is limited. At the same time, the HOMO is delocalized over the two donors and two bridges, which is easier to relax upon charging.

We now turn to the one-electron coupling elements, evaluated for all neighboring molecules as described in the Experimental Section. From the distribution of the log of the squared electronic coupling element, shown in Figure 5, we can immediately see that the holes have, on average, larger couplings (the important part of the distribution is in the area of larger couplings). Moreover, the $\log J^2$ plotted against the center-of-mass separation, bottom of Figure 5, shows large hole coupling elements even for distances up to 2.5 nm, while for electrons there is a clear exponential decay with separation and the strongest couplings are clustered around separations of ≈ 1 nm. Again, this can be traced back to the elongated shape and the D-A-D molecular architecture: for the holes, the diabatic state is localized on the edges (carbazole groups), while for the electrons, the diabatic state is on the central DBA group. It is significantly easier to have a direct contact between the molecules via the edge groups, also at larger center-of-mass separations, exactly what we observe from the distributions.

Finally, we have simulated electron and hole mobilities using the Marcus rate expression. The temperature dependence of both hole and electron mobilities is shown in Figure 6, together with the fit to the empirical temperature dependence of the mobility.^[7] Similar to the experiments, we observe balanced transport at room temperature, in spite of very different values of the energetic disorder, reorganization energies, and electronic couplings for holes and electrons. The calculated mobilities are approximately an order of magnitude smaller than the experimental values, having a similar functional temperature dependence. The reason for the discrepancy is mainly due to a small difference in energetic disorder between simulations and experiments.

4. Conclusion

We have experimentally and theoretically investigated the bulk electron- and hole-transport properties of the TADF molecule CzDBA. By using a recently developed method to form Ohmic contacts, temperature-dependent space-charge-limited currents were obtained in hole- and electron-only devices. The electron and hole mobilities and their dependence on charge concentration, electric field, and temperature were obtained by modeling the experimental current-voltage characteristics. Multiscale

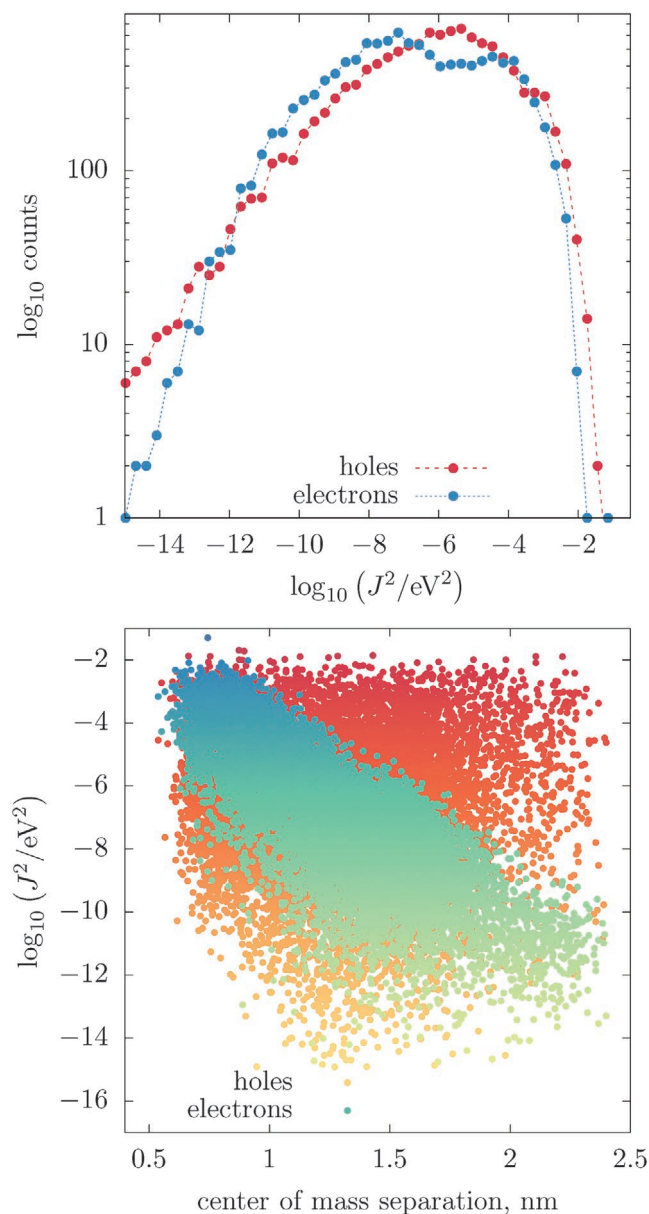


Figure 5. Distributions of squared electronic coupling elements for electrons and holes. The bottom plot shows the dependence of the logarithm of the squared electronic coupling on the center of mass separation.

simulations were carried out, which allowed to link energetic disorder, ionization energy, site spacing, and mobility to the underlying chemical structure of CzDBA.

We find that the D(onor)-B(ridge)-A(ceptor)-B(ridge)-D(onor) architecture of the TADF molecule leads to a large polarization of a cation and hence larger stabilization of the gas-phase ionization energy than electron affinity in the film. We also find that electronic coupling elements for holes are on average larger than for electrons (at the same center-of-mass separation). This is again due to the donor moieties located on the periphery of the molecule. Large HOMO/HOMO couplings balance the larger hole energetic disorder, leading to similar hole and electron mobilities, at room temperature.

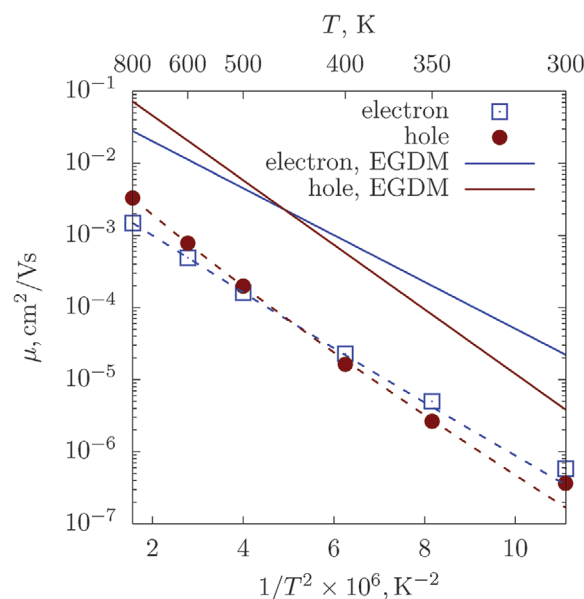


Figure 6. Simulated charge-carrier mobility with a fit to a one-dimensional Marcus-rate based mobility dependence (dashed lines). Solid lines are the EGDM mobilities extrapolated to zero density as obtained directly from the SCLC measurements. Note that SCLC measurements are performed from 213 to 295 K, and extrapolations to higher temperatures are shown only to illustrate the change in the slope of the EGDM fits. In addition, in simulations, higher temperatures help to avoid artificial trapping and finite-size effects.

Finally, both the solid-state IE and the EA (determined here as IE offset by the optical gap) fall within the trap-free window, hence we observe practically no trapping for both holes and electrons.

5. Experimental Section

Charge Transport Simulations: Hole-only devices of CzDBA were prepared on glass substrates prepatterned with indium-tin oxide. The substrates were thoroughly cleaned with detergent solution and sonication in acetone and isopropyl alcohol, followed by UV-ozone treatment. Next, a 40 nm layer of poly(3,4-ethylenedioxythiophene):polystyrene sulfonate (CLEVIOS P VP Al 4083) layer spin coated and annealed at 140 °C for 10 min in air. The substrates were then transferred into a nitrogen-filled glove box, and were not exposed to air in the subsequent steps. Subsequently, layers of MoO₃ (6 nm), C₆₀ (3 nm), CzDBA, and C₆₀ (3 nm) were thermally evaporated consecutively at base pressures below 1 × 10⁻⁶ mbar. The devices were finished with a thermally evaporated MoO₃(10 nm)/Al(100 nm).

Electron-only devices were fabricated using a similar procedure, where cleaned glass substrates were covered by thermally evaporated Al

Table 2. Molecular polarizabilities of neutral, cationic, and anionic states of CzDBA.

	α_{xx}	α_{yy}	α_{zz}	α_{xy}	α_{xz}	α_{yz}
Cation	21 865.277	702.792	364.628	0.039	0.027	-28.583
Anion	950.759	937.227	570.536	0.004	0.003	10.044
Neutral	885.747	662.490	362.003	-0.001	0.003	-13.393

Table 3. Summary of the kinetic Monte Carlo simulations.

T [K]	Electron mobility [$\text{cm}^2 \text{V}^{-1} \text{s}^{-1}$]				Hole mobility [$\text{cm}^2 \text{V}^{-1} \text{s}^{-1}$]			
	μ_x	μ_y	μ_z	μ_{aver}	μ_x	μ_y	μ_z	μ_{aver}
300	$-5.7\text{E-}07$	$-3.2\text{E-}07$	$-8.7\text{E-}07$	$-5.84\text{E-}07$	$5.8\text{E-}07$	$3.0\text{E-}07$	$2.2\text{E-}07$	$3.65\text{E-}07$
350	$-5.2\text{E-}06$	$-3.7\text{E-}06$	$-6.1\text{E-}06$	$-4.99\text{E-}06$	$3.3\text{E-}06$	$2.2\text{E-}06$	$2.4\text{E-}06$	$2.63\text{E-}06$
400	$-2.5\text{E-}05$	$-1.9\text{E-}05$	$-2.5\text{E-}05$	$-2.29\text{E-}05$	$2.1\text{E-}05$	$1.4\text{E-}05$	$1.4\text{E-}05$	$1.63\text{E-}05$
500	$-1.6\text{E-}04$	$-1.5\text{E-}04$	$-1.8\text{E-}04$	$-1.61\text{E-}04$	$2.3\text{E-}04$	$1.9\text{E-}04$	$1.8\text{E-}04$	$1.98\text{E-}04$
600	$-4.6\text{E-}04$	$-4.9\text{E-}04$	$-5.3\text{E-}04$	$-4.92\text{E-}04$	$9.0\text{E-}04$	$7.0\text{E-}04$	$7.3\text{E-}04$	$7.77\text{E-}04$
800	$-1.6\text{E-}03$	$-1.5\text{E-}03$	$-1.4\text{E-}03$	$-1.49\text{E-}03$	$3.6\text{E-}03$	$3.2\text{E-}03$	$3.1\text{E-}03$	$3.31\text{E-}03$

(35 nm) bottom electrodes. Next, layers of CzDBA and TPBi (4 nm) were evaporated consecutively, followed by evaporation of an Al (100 nm) top electrode.

The current–voltage characteristics of the devices were measured inside a nitrogen-filled glove box using a Keithley 2400 source meter.

Simulations: For morphology simulations, the OPLS-AA force field was adapted.^[20–22] All Lennard–Jones parameters were taken from this force field and the OPLS combination rules and the fudge-factor of 0.5 for 1–4 interactions were used. Atomic partial charges were computed via the CHELPG scheme.^[23] The CzDBA molecule was partitioned into five rigid fragments: two carbazole acceptors, a DBA donor in the middle, and two bridge groups in-between. The dihedral interaction potentials that connect these five fragments, shown as bold bonds in Figure 1 were parameterized as described elsewhere:^[24] for each fixed value of the dihedral angle the geometry was optimized at the m06-2x/6-311g(d,p) level. The potential difference was then fitted to the Ryckaert–Belleman polynomial, $V_{\text{rb}}(\theta) = \sum_{n=0}^5 (\cos\theta)^n$. For the C–C–N–C dihedral, the corresponding parameters were 5.932, 0.654, –19.461, –2.578, 13.046, 1.826 kJ mol^{-1} . Because of the steric hindrance from CH_3 group, the rotation of the dihedral C–B–C–C was much restricted. Thus, zeros for all the constants of this dihedral potential were used.

The long-range electrostatic interactions were treated by using a smooth particle mesh Ewald technique. A cutoff of 1.3 nm was used for the non-bonded interactions. The equations of motion were integrated with a time-step of 0.002 ps. All molecular dynamics simulations were performed in the NPT ensemble using the canonical velocity-rescaling thermostat^[25] and the Berendsen barostat^[26] as implemented in the GROMACS simulation package.^[27,28]

To obtain the *amorphous* morphology, 2048 CzDBA molecules were prearranged on a lattice and compressed (anisotropic NPT barostat) at $T = 800$ K for 1 ns. The system was then cooled to 300 K during a 1 ns run. Fast cooling froze the isotropic orientation of the high-temperature liquid, leading to an amorphous molecular ordering. In addition, a lattice crystal at 100 K was compressed, followed by a 1 ns annealing run at 600 K, and a 1 ns final cooling to 300 K. This protocol led to a *nematic* molecular ordering, with a substantial orientational ordering of molecules, as quantified in the main text.

Using the molecular dynamics trajectories, the anion, cation, and neutral state energies for each molecule in a morphology using a perturbative approach were evaluated.^[29–31] In this approach, the total energy was a sum of the gas-phase, electrostatic, and induction contributions, $E_{\text{e,h,n}} = E_{\text{e,h,n}}^{\text{gas}} + E_{\text{e,h,n}}^{\text{stat}} + E_{\text{e,h,n}}^{\text{ind}}$. To evaluate the electrostatic contribution, distributed atomic multipoles up to the fourth order were used. The induction contributions to site energies were calculated self-consistently using the Thole model^[32,33] on the basis of the atomic polarizabilities and distributed multipoles obtained by using GDMA program^[34] for a cation, anion, and a neutral molecule. All calculations were performed using the aperiodic Ewald summation scheme^[31] as implemented in the in-house developed VOTCA package.^[35]

The reorganization energies in gas phase were calculated at the m06-2x/6-311g level with Gaussian 16 program package.^[36] For electron transfer, the energy difference between the optimized anionic state and neutral state was at 7.07 eV. The relaxation energies for the anionic and

neutral states were 0.037 and 0.035 eV respectively, which resulted in a total reorganization energy of 0.072 eV for the electron transfer. For hole transfer, the energy difference between the optimized cationic state and neutral state was at –2.00 eV. The relaxation energies for the cationic and neutral states were 0.127 and 0.132 eV respectively, which led to a total reorganization energy of 0.259 eV for the hole transfer.

Electronic coupling elements were evaluated for all molecule pairs in the neighbor list using the dimer projection method^[37,38] by approximating the diabatic states of the molecular dimer with the highest occupied (lowest unoccupied) molecular orbitals (HOMO/LUMO) of the monomers. The neighbor list was constructed using a cutoff of 0.7 nm between the rigid fragments, which helped to account for the anisotropic shape of CzDBA. These calculations were performed at m06-2x/6-311g level of theory using the Gaussian 16^[36] and VOTCA^[35] packages. The calculations of gas-phase molecular polarizabilities were performed at the m06-2x/6-311g(d,p) level and are summarized in **Table 2**.

Kinetic Monte Carlo simulations for electron and hole mobilities at different temperatures were performed based on the final snapshot morphology from MD simulation, where a constant electric field of 10 000 V cm^{-1} was applied solely on either x, y, or z lattice direction, respectively. The calculated mobilities of the three directions as the estimated mobilities were averaged. The values are listed in **Table 3**.

Acknowledgements

This project received funding from the European Union Horizon 2020 research and innovation programme under Grant Agreement No. 646176 (EXTMOS). D.A. thanks the BMBF grant InterPhase (FKZ 13N13661) and the European Union Horizon 2020 research and innovation programme “Widening materials models” under Grant Agreement No. 646259 (MOSTOPHOS). This research was supported by the King Abdullah University of Science and Technology (KAUST), via the Competitive Research Grants (CRG) Program. D.A. acknowledges KAUST for hosting his sabbatical.

Conflict of Interest

The authors declare no conflict of interest.

Keywords

bipolar transport, organic semiconductors, thermally activated delayed fluorescence

Received: February 14, 2020

Revised: May 26, 2020

Published online: July 6, 2020

- [1] N. B. Kotadiya, P. W. M. Blom, G.-J. A. H. Wetzelaer, *Nat. Photonics* **2019**, *13*, 765.
- [2] T.-L. Wu, M.-J. Huang, C.-C. Lin, P.-Y. Huang, T.-Y. Chou, R.-W. Chen-Cheng, H.-W. Lin, R.-S. Liu, C.-H. Cheng, *Nat. Photonics* **2018**, *12*, 235.
- [3] H. Uoyama, K. Goushi, K. Shizu, H. Nomura, C. Adachi, *Nature* **2012**, *492*, 234.
- [4] M. Godumala, S. Choi, M. J. Cho, D. H. Choi, *J. Mater. Chem. C* **2019**, *7*, 2172.
- [5] N. B. Kotadiya, A. Mondal, P. W. M. Blom, D. Andrienko, G.-J. A. H. Wetzelaer, *Nat. Mater.* **2019**, *18*, 1182.
- [6] P. W. M. Blom, M. C. J. M. Vissenberg, *Phys. Rev. Lett.* **1998**, *80*, 3819.
- [7] A. Lukyanov, D. Andrienko, *Phys. Rev. B* **2010**, *82*, 193202.
- [8] P. Kordt, T. Speck, D. Andrienko, *Phys. Rev. B* **2016**, *94*, 014208.
- [9] P. M. Borsenberger, L. T. Pautmeier, H. Bässler, *Phys. Rev. B* **1992**, *46*, 12145.
- [10] C. Li, L. Duan, H. Li, Y. Qiu, *J. Phys. Chem. C* **2014**, *118*, 10651.
- [11] N. B. Kotadiya, H. Lu, A. Mondal, Y. Ie, D. Andrienko, P. W. M. Blom, G.-J. A. H. Wetzelaer, *Nat. Mater.* **2018**, *17*, 329.
- [12] W. F. Pasveer, J. Cottaar, C. Tanase, R. Coehoorn, P. A. Bobbert, P. W. M. Blom, D. M. de Leeuw, M. A. J. Michels, *Phys. Rev. Lett.* **2005**, *94*.
- [13] G. A. H. Wetzelaer, *AIP Adv.* **2018**, *8*, 035320.
- [14] R. Coehoorn, P. A. Bobbert, *Phys. Status Solidi A* **2012**, *209*, 2354.
- [15] M. Kuik, G.-J. A. H. Wetzelaer, H. T. Nicolai, N. I. Craciun, D. M. D. Leeuw, P. W. M. Blom, *Adv. Mater.* **2014**, *26*, 512.
- [16] P. Kordt, O. Stenzel, B. Baumeier, V. Schmidt, D. Andrienko, *J. Chem. Theory Comput.* **2014**, *10*, 2508.
- [17] M. Bouhassoune, S. L. M. van Mensfoort, P. A. Bobbert, R. Coehoorn, *Org. Electron.* **2009**, *10*, 437.
- [18] D. Abbaszadeh, A. Kunz, N. B. Kotadiya, A. Mondal, D. Andrienko, J. J. Michels, G.-J. A. H. Wetzelaer, P. W. M. Blom, *Chem. Mater.* **2019**, *31*, 6380.
- [19] A. H. Balawi, S. Stappert, J. Gorenflot, C. Li, K. Müllen, D. Andrienko, F. Laquai, *J. Phys. Chem. C* **2019**, *123*, 16602.
- [20] W. L. Jorgensen, J. Tirado-Rives, *Proc. Natl. Acad. Sci. U. S. A.* **2005**, *102*, 6665.
- [21] W. L. Jorgensen, J. Tirado-Rives, *J. Am. Chem. Soc.* **1988**, *110*, 1657.
- [22] W. L. Jorgensen, D. S. Maxwell, J. Tirado-Rives, *J. Am. Chem. Soc.* **1996**, *118*, 11225.
- [23] C. M. Breneman, K. B. Wiberg, *J. Comput. Chem.* **1990**, *11*, 361.
- [24] C. Poelking, E. Cho, A. Malafeev, V. Ivanov, K. Kremer, C. Risko, J.-L. Brédas, D. Andrienko, *J. Phys. Chem. C* **2013**, *117*, 1633.
- [25] G. Bussi, D. Donadio, M. Parrinello, *J. Chem. Phys.* **2007**, *126*, 014101.
- [26] H. J. C. Berendsen, J. P. M. Postma, W. F. van Gunsteren, A. DiNola, J. R. Haak, *J. Chem. Phys.* **1984**, *81*, 3684.
- [27] B. Hess, C. Kutzner, D. van der Spoel, E. Lindahl, *J. Chem. Theory Comput.* **2008**, *4*, 435.
- [28] S. Pronk, S. Páll, R. Schulz, P. Larsson, P. Bjelkmar, R. Apostolov, M. R. Shirts, J. C. Smith, P. M. Kasson, D. van der Spoel, B. Hess, E. Lindahl, *Bioinformatics* **2013**, *29*, 845.
- [29] A. J. Stone, *The Theory of Intermolecular Forces*, Clarendon Press, Oxford **1997**.
- [30] G. D'Avino, L. Muccioli, F. Castet, C. Poelking, D. Andrienko, Z. G. Soos, J. Cornil, D. Beljonne, *J. Phys.: Condens. Matter* **2016**, *28*, 433002.
- [31] C. Poelking, D. Andrienko, *J. Chem. Theory Comput.* **2016**, *12*, 4516.
- [32] B. T. Thole, *Chem. Phys.* **1981**, *59*, 341.
- [33] P. Th. van Duijnen, M. Swart, *J. Phys. Chem. A* **1998**, *102*, 2399.
- [34] A. J. Stone, *J. Chem. Theory Comput.* **2005**, *1*, 1128.
- [35] V. Rühle, A. Lukyanov, F. May, M. Schrader, T. Vehoff, J. Kirkpatrick, B. Baumeier, D. Andrienko, *J. Chem. Theory Comput.* **2011**, *7*, 3335.
- [36] M. J. Frisch, G. W. Trucks, H. B. Schlegel, G. E. Scuseria, M. A. Robb, J. R. Cheeseman, G. Scalmani, V. Barone, G. A. Petersson, H. Nakatsuji, X. Li, M. Caricato, A. V. Marenich, J. Bloino, B. G. Janesko, R. Gomperts, B. Mennucci, H. P. Hratchian, J. V. Ortiz, A. F. Izmaylov, J. L. Sonnenberg, D. Williams-Young, F. Ding, F. Lipparini, F. Egidi, J. Goings, B. Peng, A. Petrone, T. Henderson, D. Ranasinghe, V. G. Zakrzewski, J. Gao, N. Rega, G. Zheng, W. Liang, M. Hada, M. Ehara, K. Toyota, R. Fukuda, J. Hasegawa, M. Ishida, T. Nakajima, Y. Honda, O. Kitao, H. Nakai, T. Vreven, K. Throssell, J. A. Montgomery Jr., J. E. Peralta, F. Ogliaro, M. J. Bearpark, J. J. Heyd, E. N. Brothers, K. N. Kudin, V. N. Staroverov, T. A. Keith, R. Kobayashi, J. Normand, K. Raghavachari, A. P. Rendell, J. C. Burant, S. S. Iyengar, J. Tomasi, M. Cossi, J. M. Millam, M. Klene, C. Adamo, R. Cammi, J. W. Ochterski, R. L. Martin, K. Morokuma, O. Farkas, J. B. Foresman, D. J. Fox, *Gaussian 16 Revision B.01*, **2016**.
- [37] B. Baumeier, J. Kirkpatrick, D. Andrienko, *Phys. Chem. Chem. Phys.* **2010**, *12*, 11103.
- [38] E. F. Valeev, V. Coropceanu, D. A. da Silva Filho, S. Salman, J.-L. Bredas, *J. Am. Chem. Soc.* **2006**, *128*, 9882.